Morphological Sensitivity of Silver Nanoparticles to Environment

Nathalie Tarrat, David Loffreda

Journal Name

ARTICLE TYPE

Cite this: DOI: 00.0000/xxxxxxxxxx

Morphological Sensitivity of Silver Nanoparticles to Environment†

Nathalie Tarrat*[a] and David Loffreda*[b]

Received Date
Accepted Date

DOI: 00.0000/xxxxxxxxxx

Silver nanoparticles have been modeled by density functional theory calculations and *ab initio* molecular dynamics simulations to explore their stability in air at room temperature. The role of contaminants is considered by adsorbing monoshells of methanethiol molecules on silver nanoparticles of various morphologies (icosahedral, strongly irregular and regular truncated octahedral structures) in the range 147-201 atoms (∅ = 1.66-1.80 nm), under atmospheric nitrogen pressure. While *ab initio* molecular dynamics simulations suggest that the icosahedral and all the face-centered cubic clusters are stable at 300 K in vacuum, the ino-decahedral geometry progressively transforms into a complex structure composed of an irregularly icosahedral outershell and a decahedral core. Nanoparticle surface energies, computed at 0 K and 300 K, show a preference for FCC clusters in vacuum, as previously reported experimentally. In presence of air at 300 K, the icosahedral cluster presents the largest exothermicity in terms of adsorption surface energy of contaminant monoshells. This energetic gain is understood on the basis of the larger surface silver atomic density for the icosahedral structure, which better accommodates dense contaminant monoshells than FCC clusters. The methanethiol adlayers are composed of a complex phase of chemisorbed molecules bound to silver and in interaction with physisorbed contaminants through hydrogen bonds. This theoretical study agrees with measurements of silver nanoparticles exposed to air after synthesis in vacuum and also investigated in solution, and demonstrates that the air environment tunes the relative stability of morphologies in competition. This work paves the way on the understanding of nanoparticle ageing in environmental conditions at the atomic scale.

1 Environmental Significance

Metallic nanoparticles are widely used in industry, medicine and everyday items. These nanoparticles are then mostly released in the environment with a high power of toxicity evolving with time due to their ageing and transformations promoted by their close environment. In order to better understand their fate and propose safer working principles, an advanced knowledge of their morphology and stability in the operating environment is crucial. Theoretical modeling at the atomic scale has the power to predict their properties and fate with good accuracy, thus allowing a rational design. Silver nanoparticles are a key example of pollutants which undergo significant morphological change when exposed to air. This work tackles the difficult question of their structural evolution with time.

2 Introduction

Silver nanoparticles (Ag NPs) exposed to ambient air are globally stable as nano-objects, although they undergo significant transformations along time [1–3] and they are a major source of toxicity risks. [2,4] The ageing of Ag NPs results in the formation of many corrosion products, such as Ag_2S, Ag_2O, AgO, $AgCl$ and Ag_2SO_4. [5] According to the literature, the formation of silver sulphides on the Ag NPs surface leads to their stabilization and the subsequent modification of their general properties, in particular for thiolated Ag NPs synthesized in solution. [6–8] The presence of a sulphide surface layer suggests the existence of a direct interaction of Ag NPs and thiol contaminants (R-SH) at short timescale, when Ag NPs are first formed in vacuum and then exposed to air. According to X-ray diffraction measurements of Ag NPs (∅ = 5 nm in average size and trapped in a silica matrix exhibiting pores below 20 nm) and Ag bulk, in the temperature range of 25-700 °C, the lattice thermal expansion coefficients are much larger for Ag NPs in air by comparison with vacuum. [9] Hence, from a structural point of view, this experiment supports the idea of a strong interaction between contaminants and the nanoparticle surface,

[a] CEMES, CNRS, Université de Toulouse, 29 Rue Jeanne Marvig, 31055 Toulouse, France; Tel: +33(5) 6752 4347; E-mail: nathalie.tarrat@cemes.fr
[b] ENSL, CNRS, Laboratoire de Chimie UMR 5182, 46 allée d'Italie, 69364 Lyon Cedex, France; Tel: +33(4) 7244 8843; E-mail: david.loffreda@ens-lyon.fr

† Electronic Supplementary Information (ESI) available: [*Ab initio* molecular dynamics simulations and corresponding analyses including optimized DFT structures for the explored silver nanoparticles either in vacuum or exposed to air]. See DOI: 00.0000/00000000.

leading to a global expansion of the metal-metal bond lengths. Such a phenomenon can be understood through the formation of a surface sulphide or oxide, or through the presence of strongly adsorbed species. For thiolated Ag NPs synthesized in solution, a silver sulphide surface layer of small thickness (0.4 nm) has been measured for Ag NPs ($\varnothing$ = 3 nm) by X-ray photoelectron spectroscopy and X-ray absorption fine structure spectroscopy.[8] This thickness is twice smaller than the extension of the organic thiol allyl mercaptan coating (0.8 nm). According to the authors, this silver sulphide corresponds to a single subsurface sulphur layer, of which the structure recalls a body-centered cubic Ag_2S phase (similar to argentite β-Ag_2S[10,11]). Up to date, the nature of such an interaction between Ag NPs (synthesized in vacuum) and thiol molecules under air exposure remains to be elucidated.

In general, Ag NPs offer a large variety of interesting properties, which usually depend on the nanoparticle size, shape and functionalization, in various application domains such as antibacterial fighting,[12–14] catalysis[15,16] or optics.[17,18] In the experimental literature, the morphology of Ag NPs, synthesized in vacuum[19–21] or in solution,[22] has already been investigated for specific sizes. In particular, for a size of $Ag_{309\pm7}$ synthesized and characterized by High-Angle Annular Dark-Field Scanning Transmission Electron Microscopy (STEM-HAADF) in vacuum, the authors have shown that the face-centered cubic (*FCC*) clusters are dominating statistics,[20] while the icosahedral forms are largely minority. When Ag NPs are synthesized in vacuum in the range 1-3000 atoms and exposed to air before characterization, icosahedral clusters are competitive with other symmetries in the range 201-400 atoms and prevalent for any other size.[21] This latter experimental result observed recently at the contact with air is consistent with previous measurements of $Ag_{312\pm55}SR_{84}$ synthesized in solution and characterized by STEM-HAADF in dried conditions.[22] The proportion of decahedral forms progressively increases with the NP size in vacuum, by comparison with *FCC* and icosahedral clusters.[19] In contrast, after air exposure, the decahedral clusters are either competitive or majority in the range 201-500 atoms, and minority at very small and large size.[21] In solution, the observations are again different since the decahedral forms are absent for $Ag_{312\pm55}SR_{84}$.[22] Hence, the working environment plays a key role on the competition between structures. The relationship between morphology statistics and exposure to ambient air is not understood so far.

A relevant approach to investigate the difficult question of structural competition is the theoretical modeling at the atomic scale. Among the methods, atomic potentials of non-bonded interactions between silver atoms have been developed to tackle the study of the relative competition between the three classical symmetries (octahedral, icosahedral, decahedral): many-body potentials (tight-binding, embedded atom model, Gupta, Sutton–Chen) and pairwise Lennard-Jones potentials.[23–28] From a static standpoint, these potentials have been used in global optimization methods[29–33] and they have shown the predominance of decahedral clusters in a large range of size, with a few exceptions in favor of icosahedral forms. This result, obtained in vacuum, agrees neither with Ag NPs synthesized and characterized in vacuum,[19,20] nor with Ag NPs exposed to air[21] or studied in solution.[22] Apart from the question of morphology, semi-empirical potentials have been combined with classical molecular dynamics to study the interaction of Ag NPs with synthesis ligands, surfactants and liquid water,[25–28] and of extended silver surfaces with various adsorbates.[23,24]

More accurate theoretical methods such as Density Functional Theory (DFT) have been used for exploring the question of the morphology of Ag NPs in vacuum at a given size[20] but also the single adsorption properties of carbon monoxide and methylthio radicals on Ag NPs of various symmetries in the range 13-309 atoms[34,35] and on extended silver surfaces.[36,37] A few studies have been devoted to the optical properties of thiolated silver clusters in the range 44-211 atoms, predicted by time-dependent DFT calculations.[38,39] In the case of isolated silver clusters in vacuum at the size 309$\pm$7 atoms, DFT calculations including dispersion have shown that *FCC* morphologies prevail over icosahedral and decahedral shapes, in close agreement with measurements.[20] Regarding single adsorption of methylthio radicals, Becerril and Noguez have shown that adsorption strength poorly depends on the icosahedral nanoparticle size from 55 to 309 atoms, by combining a generalized gradient approximation (GGA) functional without dispersion with localized basis sets.[35] They have reported on an unexpected expansion of the core metal-metal distances, in parallel with a contraction of the surface metal-metal bonds, which contrasts with the first conclusions based on interatomic potentials simulations.[40] The single adsorption of carbon monoxide has been compared on cuboctahedral, icosahedral and classical decahedral clusters in the range 54-309 atoms at the GGA RPBE level including dispersion corrections (Grimme-D3 method).[34] The adsorption strength is globally weak and dominated by dispersion. The adsorption is the largest one on decahedral and cuboctahedral Ag NPs and the weakest one on icosahedral aggregates. In addition, *ab initio* molecular dynamics (AIMD), employed to explore the structure of one Ag_{54} cluster deposited on an alumina surface (in the range 25-100 K, with a total integration time of 1.2 ps), has shown the existence of amorphous and five-fold symmetric clusters in contact with the support. Up to date, AIMD has not been considered to determine the effect of a complex chemical environment on the morphology of silver nanoparticles, such as air exposure.

In this work, we report on theoretical models of the early stage exposure of Ag NPs to ambient air by combining AIMD simulations and geometry optimizations, on the basis of dispersion-corrected DFT calculations. To do so, we have explored separately and synergistically three environmental effects : temperature, air pressure and chemical contamination through methanethiol molecules. In particular, we have investigated the evolution of structural and energetic properties of Ag NPs in the range 1.66-1.80 nm, at the timescale of a few ps provided by the AIMD simulations. These environment effects have been compared for three typical morphologies (octahedral, icosahedral and decahedral symmetries), interpreted and discussed by comparison with measurements.

3 Methodology

DFT calculations were performed by using the VASP code together with the PBE-D3 semi-empirical dispersion-corrected functional in its zero-damping formalism[41–44] which was chosen to predict correctly cohesion energies and weak van der Waals forces.[20] The interactions between electrons and ion cores were described by potentials generated by the Projector Augmented-Wave method (11 valence electrons per Ag, 6 per S and 4 per C atoms).[45] Valence electrons were described with plane wave basis sets in tight conditions (with a kinetic cutoff energy of 400 eV). A large simulation box ($50\times50\times50$ Å^3) was used in order to ensure a vacuum space of at least 3.2 nm between periodically equivalent nanoparticles. For the NP models, the Brillouin zone sampling in reciprocal space corresponds to the Γ point. For dealing with the partial occupancies, a Methfessel–Paxton smearing was used with σ of 0.2 eV. The geometry of the complete systems was relaxed without constraint, with a tight convergence criterion of 10^{-6} eV for the total electronic energy, until each residual force on nuclei was less than ±0.01 eV.Å^{-1}. Similar computational conditions were used for calculating the reference of an isolated methanethiol molecule. For Ag bulk reference, the grid of the Brillouin zone used for determining the total electronic energy was $37\times37\times37$ k-points for the primitive rhombohedral cell.

Concerning AIMD simulations (see † for details of all the trajectories, and Table S1 for a summary of all the computational conditions), two different models were considered : vacuum and air exposure. Clean Ag NPs in vacuum were equilibrated at 300 K and at 600 K in the same 3D box of 125 nm^3, with a cutoff energy of 250 eV. The thermalization and equilibration were performed by using a velocity rescaling thermostat associated with a timestep of 4 fs at 300 K and 2 fs at 600 K, for a total integration time in the range 16-20 ps at 300 K and 10-19 ps at 600 K. Regarding air exposure, atmospheric pressure has been modeled by equilibrating a pure N_2 gas at 300 K in a 3D box of 125 nm^3, corresponding to a pressure of 5 atm (*i.e.* 15 N_2 molecules). The total integration time was 60 ps with a timestep of 2 fs. Another AIMD simulation at 300 K was performed by developing a *FCC* bulk model composed of 32 Ag atoms in the supercell (total electronic energy being computed with a $13\times13\times13$ k-point mesh), with the same thermostat, over a total integration time of 16 ps (with a timestep of 4 fs). The immersion in air of Ag NPs decorated by a contaminant monoshell was performed by extracting a pure gaseous nitrogen configuration after AIMD equilibration at 300 K, quenching the corresponding structure and interfacing this optimal gas with contaminated Ag NPs. Then, all the corresponding interfaces between Ag NPs and gaseous nitrogen were completely optimized in tight conditions, before being equilibrated by AIMD. For the immersed NP, whatever its size, the number of N_2 molecules is kept constant, since the accessible volume (125 nm^3) is not significantly reduced by the presence of the Ag NP. For each trajectory, the equilibration at 300 K was performed by using a velocity rescaling thermostat (with a small timestep of 1 fs) during 7 ps in total (*i.e.* 7000 structures per trajectory). At the end of those AIMD simulations, three structures of complete systems (contaminated Ag NPs and gaseous nitrogen) were selected and quenched in tight geometry optimization conditions. Finally, further geometry optimizations of contaminated Ag NPs were carried out without the nitrogen gas, by starting from the optimal structures obtained at the previous step. For comparing the stability of nanoparticles in vacuum at 300 K, the excess energy normalized to the NP surface area was calculated by averaging the potential energy of the clean NPs over the last 2 ps of the AIMD trajectories (500 structures). The potential energy of the *FCC* bulk reference at 300 K was also averaged over the last 2 ps of the AIMD simulation (500 structures).

4 Results and discussion

4.1 Temperature effects on Ag NPs in vacuum

In this work, Ag NPs have been explored in the range 147-201 atoms (∅ = 1.66-1.80 nm). Models of the three key symmetries (*Ih*, *D5h* and *FCC*) have been considered with Mackay icosahedral (Ag147ico, *Ih*), ino-decahedral (Ag147ino, *D5h*), cuboctahedral (Ag147cubo, *FCC*), strongly irregular (Ag147sito, *FCC*) and regular (Ag201rto, *FCC*) truncated octahedral forms. Ag147sito belongs to a new interesting family of strongly irregular *FCC* clusters exhibiting (100) and (111) facets of various size and shape†. In vacuum and without temperature effects, the relative stability of the clusters has been determined by the excess energy normalized to the nanoparticle surface area (noted γ_{NP} in Figure 1), from DFT calculations at 0 K, as previously proposed for Ag NPs:[20]

$$\gamma_{NP} = \frac{E_{tot}^{NP} - N_{at}E_{at}^{bulk}}{\mathscr{A}} \quad (1)$$

with E_{tot}^{NP} being the total electronic energy of the clean nanoparticle, N_{at} the number of Ag atoms, E_{at}^{bulk} the total electronic energy per Ag atom in the bulk and $\mathscr{A}$ the nanoparticle surface area calculated from the optimized nanoparticle geometry (see[20] for details related to area calculation). According to these DFT calculations, the truncated octahedral clusters (Ag201rto and Ag147sito, 0.809/0.835 J.m^{-2}, respectively) present a lower γ_{NP} than Ag147ico (1.051 J.m^{-2}), Ag147ino (1.076 J.m^{-2}) and Ag147cubo (1.076 J.m^{-2}). These values are compatible with experiments of nanoparticle surface energy (1.13 J.m^{-2}, see[46,47]) and with microscopic observations at a larger size.[20]

To explore temperature effects in vacuum, we have selected at least one cluster of each key symmetry (Ag147ico, Ag147ino and Ag147sito) and for the most stable family (*FCC*) we have considered the size effect (Ag201rto). AIMD simulations have been performed by integrating time up to 20 ps at 300 K, and up to 19 ps at 600 K (depending on the stability of the clusters). The average excess energy normalized to the nanoparticle surface area (noted $<\gamma_{NP}>$ in Figure 1) has been calculated over the last two picoseconds† of each trajectory at 300 K as follows:

$$<\gamma_{NP}> = \frac{<E_{tot}^{NP}> - N_{at}<E_{at}^{bulk}>}{\mathscr{A}} \quad (2)$$

with $<E_{tot}^{NP}>$ being the average total electronic energy of the clean nanoparticle at 300 K, $<E_{at}^{bulk}>$ the average total electronic energy per Ag atom in the bulk at 300 K and $\mathscr{A}$ the nanoparticle surface area as calculated previously. At 300 K,

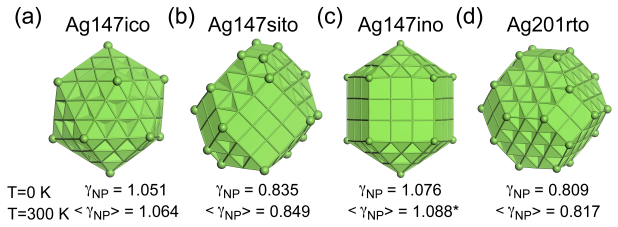

Fig. 1 Illustration of Ag NPs in vacuum at various size and morphology according to DFT calculations and AIMD simulations at 300 K. Clean Ag NPs calculated at 0 K and in vacuum are depicted in (a) regular Mackay icosahedron Ag147ico (*Ih* symmetry, $\varnothing = 1.66$ nm), (b) strongly irregular truncated octahedron Ag147sito (*FCC*, $\varnothing = 1.70$ nm), (c) regular inodecahedron Ag147ino (*D5h* symmetry, $\varnothing = 1.67$ nm) and (d) regular truncated octahedron Ag201rto (*FCC*, $\varnothing = 1.80$ nm). Excess energies normalized to NP surface area are reported and expressed in $J.m^{-2}$ at 0 K from DFT calculations and at 300 K from AIMD simulations. The values at 300 K have been averaged over 2 ps of the AIMD trajectories (i.e. over 500 structures) †. In the case of Ag147ino, the star means that the average concerns the structure transformed at 300 K (see Figure S4†). The color label for Ag atoms is green. The vertices are represented by balls, whereas the bonds between Ag atoms are depicted by joint sticks.

Ag147ico, Ag147sito and Ag201rto are stable morphologies, in the considered total integration time†, whereas Ag147ino transforms rapidly into a complex structure mixing a quasi-decahedral symmetry in the core and an icosahedral-like symmetry in the outer shell. The stability order predicted at 300 K and based on average excess energies is identical to the one proposed at zero temperature, i.e. *FCC* clusters being more stable. At 600 K, only the Ag147ico and Ag201rto clusters remain stable along the AIMD trajectories†; Ag147sito transforms progressively into a complex multi-domain cluster combining *FCC* symmetry and concave fragments, while Ag147ino transforms into a strongly distorted Ag147ico cluster presenting a surface adatom. As a preliminary conclusion, temperature effects in vacuum are strong since they offer the possibility either to change the surface of the cluster (Ag147ino at 300 K, Ag147sito at 600 K) or to completely transform a given symmetry into another one (Ag147ino at 600 K). According to all the explored AIMD trajectories at 300 and 600 K, no amorphous cluster has appeared.

4.2 Zero-temperature adsorption of contaminants on Ag NPs in vacuum and under nitrogen pressure

Methanethiol molecule has been selected as a relevant contaminant model for investigating the effect of air exposure onto three competitive morphologies (Ag147ico, Ag147sito and Ag201rto), because of their intrinsic stability at room temperature, as demonstrated in the previous section. A recent combined experimental and theoretical study shows an almost equivalent proportion of highly symmetric and amorphous Ag NPs in the range 1-3000 atoms, when they are synthesized in vacuum and exposed to air.[21] In our Heuristic approach, we are interested in investigating the families of symmetric nanoclusters. Since too strongly adsorbed species likely lead to the deformation of Ag NPs, in particular in the considered range of sizes (below 1.8 nm), one has to choose a moderately bound contaminant to keep the cluster high symmetries. When Ag NPs are exposed to air, contaminants of various chemical nature can adsorb at their surface, especially atomic oxygen or methylthio radical (CH3S*) in the family of sulphides, through O_2 or methanethiol dissociations. The adsorption strength is directly linked to the chemical bonding formed between Ag NP and contaminant, which is expressed by the binding energy referred to contaminant in the gas phase (atom or radical species). According to previous theoretical studies of methylthio adsorption on Ag NPs in the range 13-309 atoms (binding energies from -2.35 to -1.19 eV/molec[35]) and on Ag(111) extended surface (binding energies from -1.5[37] to -0.9 eV/molec[35]), this radical species is a strongly bound adsorbate. Concerning the dissociative adsorption of molecular oxygen, most of the previous theoretical studies address adsorption energies instead of binding energies. The adsorption energies correspond to the energetic balance between the gain due to adsorption of atomic oxygen (effective binding energy) and the loss due to gas phase dissociation of O_2, hence giving moderate energetics and a misleading impression of mild binding.[48,49] This being said, a few studies have reported on the binding energy of atomic oxygen on silver referenced to gas phase oxygen atom.[50–52] On Ag_{13} cluster, this binding energy is really large (-3.5 eV/atom[51]). This is equivalent when atomic oxygen is adsorbed on Ag(111) at low coverage ($\approx$ -3.5 eV/atom)[50–52] and this remains strong even at saturation ($\approx$ -2 eV/atom for 1 ML).[50] Hence, the two likely candidates for modeling Ag NPs contamination are strongly bound species, even at high coverage for atomic oxygen. In such conditions, Ag NPs in the range 147-201 atoms are expected to be significantly deformed upon such contaminant adsorption, leading to a crystalline symmetry loss. For all these reasons, the choice of a molecule such as methanethiol (CH3SH) is relevant to interpret the isomeric change of Ag NPs observed experimentally for classical symmetries,[21] thanks to its moderate binding energy, as demonstrated in the following.

Isolated adsorption shows a large variety of chemisorption structures, mainly $\eta_1\mu_1$ or top adsorption structure†(see Table 1), with a chemical bonding between the sulphur atom and one surface Ag atom. Interestingly, all these forms present a similar adsorption energy per molecule (for instance for the most stable structures, -0.627 eV for Ag147ico, -0.697 eV for Ag147sito, -0.667 eV for Ag201rto) corresponding to a moderate bonding strength, as expected. The adsorption depends on the nature of the interaction site (vertex, edge or facet). Especially, the balance between covalence (short-range interactions) and dispersion (long-range van der Waals interactions) is mainly determined by the proximity between the methyl group of methanethiol and the Ag surface. In the case of adsorption on (100) and (111) facets, whatever the Ag NP, the dispersion contributions are dominating the adsorption energy, as reported in Table 1 (52-73%). For adsorption on edges and vertices, such contributions are much lower (28-51%). The amount of dispersion correlates also with the length of the Ag-S distance.

Based on this systematic study of isolated adsorption, DFT models of homogeneous chemisorption shells of methanethiol covering

Table 1 Isolated adsorption of methanethiol on Ag NPs. Adsorption sites are defined on Ag147ico, Ag147sito and Ag201rto. Adsorption energy E_{ads} (eV), contribution of dispersion on adsorption energy E_{ads}^{disp} (eV and %) and bond length between Ag and S at the adsorption site d_{Ag-S} (Å). Each adsorption structure is illustrated in a figure† of which the corresponding number is reported in this table.

NP	Adsorption site	Figure†	E_{ads}	E_{ads}^{disp}	E_{ads}^{disp}(%)	d_{Ag-S}
Ag147ico	(111)	S10	-0.601	-0.371	62	2.672
	Vertex	S10	-0.559	-0.180	32	2.595
	Edge	S10	-0.627	-0.318	51	2.628
Ag147sito	(100) 16 atoms	S11	-0.636	-0.390	61	2.658
	(100) 12 atoms	S11	-0.679	-0.380	56	2.626
	(100) 9 atoms	S11	-0.697	-0.364	52	2.617
	(111) 21 atoms	S11	-0.599	-0.435	73	2.691
	(111) 9 atoms	S11	-0.603	-0.361	60	2.663
	Vertex	S11	-0.637	-0.178	28	2.562
	Vertex (neighbor of 1 vertex)	S11	-0.664	-0.239	36	2.577
	Vertex (neighbor of 2 vertices)	S11	-0.633	-0.215	34	2.578
	Vertex (on a 4 atoms (100) facet) - Bridge position	S11	-0.430	-0.196	46	2.789/2.840
	Edge (111)|(100)	S11	-0.627	-0.277	44	2.590
	Edge (111)|(111)	S11	-0.644	-0.278	43	2.577
Ag201rto	(100)	S12	-0.663	-0.368	55	2.627
	(111) center	S12	-0.621	-0.436	70	2.712
	(111) middle layer	S12	-0.596	-0.399	67	2.703
	Vertex	S12	-0.666	-0.222	33	2.569
	Edge (111)|(100)	S12	-0.667	-0.316	47	2.612
	Edge (111)|(111)	S12	-0.616	-0.261	42	2.601

Ag NPs have been optimized in vacuum, as illustrated in Figure 2 for the most stable configurations (several cases of coadsorption structures have been considered†). The weak change of stability from the most stable structures to metastable ones invites us to generate coadsorption shells covering Ag NPs, by maximizing the most competitive forms and completing the adlayers with metastable structures. Not to induce a bias in the whole stability of the contaminated Ag NPs, we have chosen very similar surface coverage for the three clusters (0.33-0.36 ML as depicted in Figure 2 and corresponding to 32, 32 and 44 molecules on Ag147ico, Ag147sito and Ag201rto, respectively). For Ag147ico and Ag201rto, we have considered two different initial coadsorption configurations defined as structure "1" and "2" in table 2. In the case of Ag147ico, the number of contaminants is the same (32 molecules) whereas in the case of Ag201rto, the number of methanethiol changes from 40 (0.33 ML) to 44 (0.36 ML) molecules. The change of number of contaminants for Ag201rto results from its morphology and the principle of maximizing the most competitive adsorption forms. After geometry optimizations, the adlayers of contaminants are weakly modified. Top coadsorption structures are kept at various sites including vertices, edges and facets. A few chemisorbed contaminants share a hydrogen bond. No desorption or physisorption is seen meaning that the considered coverage is below saturation.

From a quantitative standpoint, to compare the adsorption properties between nanoparticles of different morphology and size, the stability of the contaminant shells on Ag NPs is evaluated by calculating the total coadsorption energy normalized to the Ag NP surface area (noted Γ_{coads} and expressed in J.m^{-2}):

$$\Gamma_{coads} = \frac{E_{tot}^{NP@N_{cont}} - E_{tot}^{NP} - N_{cont}E_{tot}^{cont}}{\mathscr{A}} \quad (3)$$

$E_{tot}^{NP@N_{cont}}$ being the total electronic energy of the Ag cluster contaminated by N_{cont} methanethiol molecules, E_{tot}^{cont} the total electronic energy of an isolated contaminant molecule. Corresponding values have been exposed in Table 2. In addition, to evaluate the adsorption strength of contaminant shells, their average coadsorption energy on Ag NPs per methanethiol can then be derived as follows:

$$E_{coads} = \frac{E_{tot}^{NP@N_{cont}} - E_{tot}^{NP} - N_{cont}E_{tot}^{cont}}{N_{cont}} \quad (4)$$

Surface silver atomic densities of Ag NPs (noted SSD) can be calculated by counting the number of Ag surface atoms normalized to the nanocluster surface area, as well as molecule surface densities (noted MSD) obtained by normalizing N_{cont} by the same area (see Table 2).

A first remark concerns the differences in the trends between SSD and the number of Ag surface atoms in the two considered Ag147 clusters. In fact, Ag147ico and Ag147sito have the same total number of Ag atoms, although Ag147sito has 4 additional surface atoms (96 *vs* 92 atoms). The SSD of Ag147sito, of which the surface is composed a mixture of (111) and (100) facets, is however lower than that of Ag147ico, which is composed exclusively of (111) facets (6.130 *vs* 7.733 atom.nm^{-2}, respectively). An identical total number of methanethiol contaminants (32) has been considered for the coadsorption shells on both Ag147ico and Ag147sito clusters, thus allowing the comparison of total electronic energies between them. Note in passing that the trends coming from the analysis of total electronic energies can not be compared to those obtained from average coadsorption energies E_{coads} (see Table 2), since the latter ones are calculated from different references (i.e. each clean silver nanocluster). DFT calculations show that the coadsorption structures on Ag147ico are more stable than the one on Ag147sito by roughly 3 eV in total electronic energy, thus suggesting a preference for the contami-

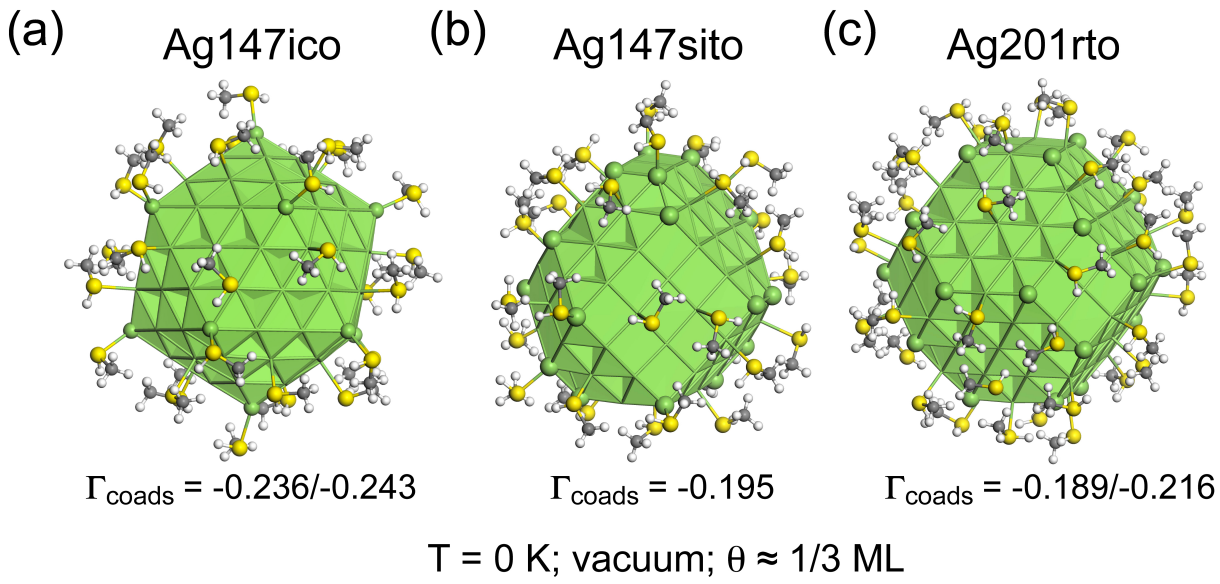

Fig. 2 Illustration of Ag NPs contaminated by shells of coadsorbed methanethiol molecules, after geometry optimizations at 0 K and in vacuum: (a) 32 contaminants coadsorbed on Ag147ico, (b) 32 molecules on Ag147sito and (c) 44 methanethiol on Ag201rto (corresponding to a surface coverage $\theta \approx 1/3$ ML, ML = monolayer). Total coadsorption energies normalized to the nanoparticle surface area (Γ_{coads}, in J.m^{-2}) are reported with ranges of values corresponding to Table 2. The color labels are green for Ag, yellow for S, gray for C and white for H atoms.

Table 2 Coadsorption structures in vacuum at 0 K for contaminated Ag NPs (Ag147ico, Ag147sito and Ag201rto). Name of coadsorption structure, number of corresponding figure†, number of methanethiol molecules in the adsorbed layer (N_{HSCH3}), number of surface Ag atoms in the clusters ($N_{Ag,surf}$), surface silver atomic densities (SSD, atom.nm^{-2}), molecule surface densities (MSD, molec.nm^{-2}), surface coverage (θ, ML = monolayer), average coadsorption energy (E_{coads}, eV/molec), average contribution of dispersion to coadsorption energy (E^{disp}_{coads}, eV/molec and %) and total coadsorption energy normalized to nanoparticle surface area (Γ_{coads}, J.m^{-2}).

NP	Coads. Structure	Figure†	N_{HSCH3}	$N_{Ag,surf}$	SSD	MSD	θ	E_{coads}	E^{disp}_{coads}	E^{disp}_{coads}(%)	Γ_{coads}
Ag147ico	1	S13	32	92	7.733	2.690	0.35	-0.549	-0.347	63	-0.236
	2	S14	32	92	7.733	2.690	0.35	-0.565	-0.333	59	-0.243
Ag147sito		S15	32	96	6.130	2.043	0.33	-0.596	-0.376	63	-0.195
Ag201rto	1	S16	40	122	6.225	2.041	0.33	-0.580	-0.358	62	-0.189
	2	S17	44	122	6.225	2.245	0.36	-0.601	-0.380	63	-0.216

nated icosahedral isomers at zero temperature. Regarding Γ_{coads}, the energetic gain due to the coadsorbed contaminant shell on the Ag147ico cluster (-0.243 J.m^{-2}) is larger than the ones of the preferential cordsorption structures found for *FCC* clusters (-0.195 J.m^{-2} for Ag147sito and -0.216 J.m^{-2} for Ag201rto). We note that the Γ_{coads} ranges of icosahedral and *FCC* shapes are not overlapping (cf. Table 2), thus meaning a clear preference of contamination for Ag147ico. Hence, for Ag147 nanoparticles, the trends in Γ_{coads} (energetic gain due to contamination) are compatible with those in total electronic energies (absolute stability). The variations of molecule surface densities (MSD) are also correlated with the trends in Γ_{coads} since they follow those of surface silver atomic densities (SSD).

Concerning E_{coads}, the trend is opposite since the average coadsorption energy is more exothermic on Ag147sito (-0.596 eV/molec) than on Ag147ico (from -0.549 to -0.565 eV/molec). This discrepancy is not surprising since both descriptors are averaged differently, as explained before. Note in passing that the weight of dispersion on adsorption energetics is identical (63%) for the three most stable contaminated clusters (Ag147ico, Ag147sito and Ag201rto), thus indicating that the long-range van der Waals interactions are not ruling the differences.

In this work, we aim to probe the change of statistics of existing Ag NPs synthesized in vacuum, upon air exposure. Then we propose to evaluate the energetic gain due to contamination from one nanocluster to another one. Our assumption related to the morphology changes is based on thermodynamic considerations, meaning that kinetic trapping is not limiting. In order to take into account morphology, size of the Ag NP and accessible nanoparticle surface area to contaminants, we have selected Γ_{coads} as the relevant descriptor for this analysis.

In the next models, the effect of the pressure of nitrogen gas on the contaminated Ag NPs is explored at 0 K (see Figure 3 for the most stable structures). The gas/nanoparticle interface is resulting from the combination of DFT optimal coadsorption structures exposed in Figure 2 and a 3D box of N2 molecules (see † and also the methodology section for the description of the gas model). After geometry optimizations at 0 K, no significant configurational change is observed in the contaminant shells. The

interaction between gaseous nitrogen and contaminated Ag NPs is rather weak through long-range dispersion interactions. Only a few N_2 molecules are physisorbed. This pressure effect appears in a systematic and small increase (about 0.002 J.m^{-2} in absolute value) of the total coadsorption energy normalized to the nanoparticle surface area *in presence of nitrogen* which is noted $\tilde{\Gamma}_{coads}$ and calculated as follows:

$$\tilde{\Gamma}_{coads} = \frac{E_{tot}^{NP@N_{cont}@15N_2} - E_{tot}^{NP} - N_{cont}E_{tot}^{cont} - E_{tot}^{15N_2}}{\mathscr{A}} \quad (5)$$

where $E_{tot}^{NP@N_{cont}@15N_2}$ is the total electronic energy of the optimized complete system including the Ag NP, the contaminant shell and the nitrogen equilibrated gas, and $E_{tot}^{15N_2}$ is the total electronic energy of the optimized 3D box of 15 N_2 molecules resulting from the equilibrated nitrogen gas †.

4.3 Temperature and pressure effects on contaminated Ag NPs

In the following section, the temperature effects are explored by AIMD simulations at 300 K for contaminated Ag NPs immersed in the gaseous nitrogen 3D box (starting from optimized structures obtained in the previous section and presented in Figure 3). Each considered coadsorption structure of the three Ag NPs has been explored from AIMD simulations (see Table 3). The total integration time is 7 ps per trajectory, thus exploring 35000 structures in total†. After the thermalization step, which lasts in average 2 ps, three configurations per trajectory have been extracted from the lowest potential energy wells and then quenched to zero temperature by optimizing them in accurate conditions (see Methodology section). The corresponding notations and energetics are reported in Table 3. The most stable optimized structures resulting from AIMD simulations have been presented in Figure 4, as well as the related $\tilde{\Gamma}_{coads}$.

From a general standpoint, the complex combination of temperature, pressure and contaminant effects does not induce a significant change of the morphology of the three considered Ag NPs, in the limit of the total integration time. Among all the AIMD simulations, the methanethiol molecules stay adsorbed on Ag NPs (except one single desorption event registered during the thermalization step of Ag147ico coadsorption structure 2), thus meaning that the coverage considered in all the systems is constant throughout the simulations and below saturation. Very interestingly, no dissociation of the SH bond of any contaminant has been observed, hence proving the molecular stability of methanethiol on Ag NPs at room temperature and under a nitrogen gas pressure. The formation of methanethiolates seems to require other conditions (for instance, a higher temperature, a co-contaminant species or a different electronic state for Ag NPs). In addition, for gaseous nitrogen, no molecular or dissociative chemisorption has been seen, although a few molecules are physisorbed at the proximity of contaminated Ag clusters through long-range van der Waals interactions. Concerning the contaminant shells, a strong reorganization of the adsorbates is systematically observed during AIMD. Instead of keeping a homogeneous and well-organized chemisorption layer of methanethiol, we have found a complex mixture of three adsorption forms : top chemisorption through S-Ag bond, non-conventional adsorption through unusual hydrogen bond (hydrogen atom of SH moiety pointing toward the Ag cluster, see figure 4) and physisorption. An original coadsorption motif is seen many times between two or three contaminants chemisorbed on top sites and bound through hydrogen bonds with a third or a fourth methanethiol molecule. This latter is adsorbed on Ag NPs via one non-conventional hydrogen bond (see pink dotted thick lines and developed views on Figure 4 for examples). The particular coadsorption form involving one non-conventional hydrogen $H\cdots Ag$ bond and two $HS\cdots HS$ hydrogen bonds is isoenergetic to an isolated top chemisorption structure (in total electronic energy). Hence the observed reorganization at 300 K may be ruled by entropic gain of non-conventional hydrogen-bonded contaminants which are more free to translate and rotate than chemisorbed molecules. This results in a small increase of $\tilde{\Gamma}_{coads}$ as shown in Figure 4 and Table 3.

The average coadsorption energy per contaminant E_{coads} and the coadsorption energy normalized to NP surface area $\tilde{\Gamma}_{coads}$ have been reported on Table 3. Likewise zero temperature, Ag147ico presents the larger $\tilde{\Gamma}_{coads}$, whatever the structure extracted from AIMD and quenched at 0 K. The energetic gain ranges from -0.263 to -0.252 J.m^{-2}. The adsorption exothermicity on *FCC* clusters is globally less favorable than the one on the icosahedral form, with a slight preference for Ag201rto (from -0.235 to -0.209 J.m^{-2}) over Ag147sito (from -0.204 to -0.203 J.m^{-2}). An energy decomposition analysis is proposed to explain such an energy gain (cf Table 3), by evaluating the Ag NP deformation energy induced by the contaminant shell $\tilde{\Gamma}_{def}^{NP}$ and the interaction energy between the contaminant shell and the Ag NP $\tilde{\Gamma}_{int}^{NP-shell}$ (*i.e.* chemical bonding) calculated as follows:

$$\tilde{\Gamma}_{coads} \approx \tilde{\Gamma}_{int}^{NP-shell} + \Sigma\tilde{\Gamma}_{def} \quad (6)$$

$$\tilde{\Gamma}_{int}^{NP-shell} = \frac{E_{tot}^{NP@N_{cont}@15N_2} - E_{tot}^{NP@\varnothing@\varnothing} - E_{tot}^{\varnothing@N_{cont}@\varnothing} - E_{tot}^{15N_2}}{\mathscr{A}} \quad (7)$$

$$\tilde{\Gamma}_{def}^{NP} = E_{tot}^{NP@\varnothing@\varnothing} - E_{tot}^{NP} \quad (8)$$

with $\Sigma\tilde{\Gamma}_{def}$ being the sum of the deformation energies of the contaminant shell and of the Ag NP between their optimized geometry in the adsorbed system and the one in their isolated thermodynamic state, $E_{tot}^{NP@N_{cont}@15N_2}$ being the total electronic energy of the whole optimized system, $E_{tot}^{\varnothing@N_{cont}@\varnothing}$ and $E_{tot}^{NP@\varnothing@\varnothing}$ being the single point energies of the contaminant shell and of the Ag NP cluster, extracted separately from the complete optimized system, respectively. In Eq. 6, the approximation is related to the neglect of the interaction terms corresponding to the presence of the third component of the complete system (gas phase N_2). Hence $\tilde{\Gamma}_{int}^{NP-shell}$ is defined as a two-body interaction term (Eq. 7), evaluated from the optimal structures of the fragments obtained in presence of N_2, but in absence of N_2 for total electronic energy calculations.

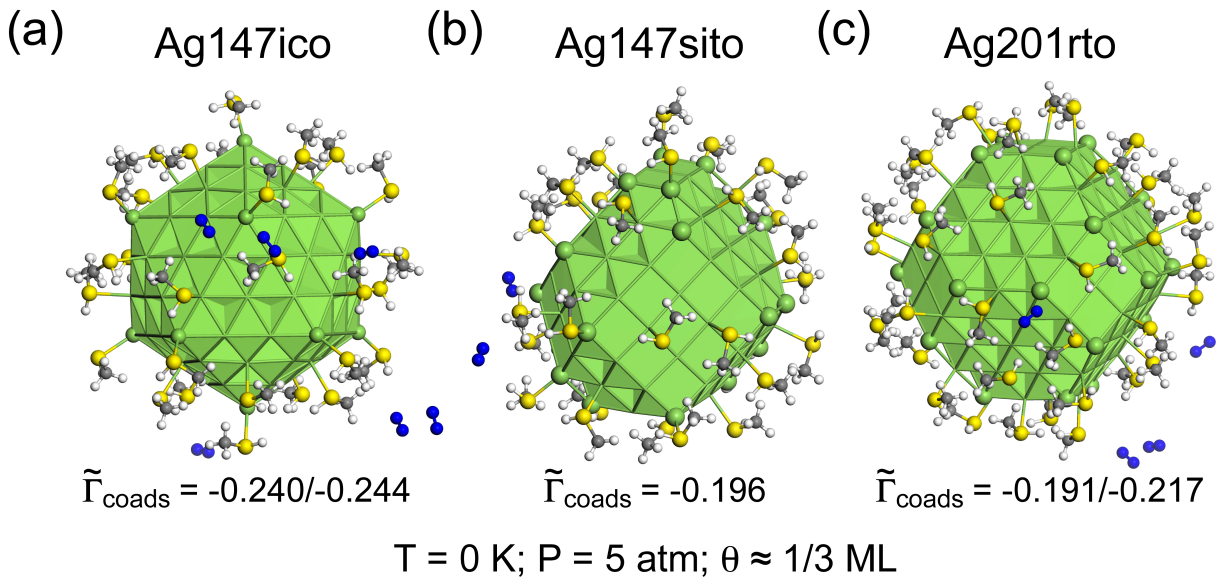

Fig. 3 Illustration of Ag NPs contaminated by shells of coadsorbed methanethiol molecules after geometry optimizations at 0 K under nitrogen pressure†. The numbers of contaminant molecules are identical to those exposed in Figure 2: (a) Ag147ico, (b) Ag147sito and (c) Ag201rto. Total coadsorption energies normalized to the nanoparticle surface area ($\tilde{\Gamma}_{coads}$, in J.m^{-2}) are reported with ranges of values corresponding to several coadsorption structures†. The color labels are green for Ag, yellow for S, blue for N, gray for C and white for H atoms.

According to this analysis, the predominant contribution is the interaction energy between the contaminant shell and the Ag NP $\tilde{\Gamma}_{int}^{NP-shell}$ (-0.231 J.m^{-2} for Ag147ico, -0.185 J.m^{-2} for Ag147sito and -0.210 J.m^{-2} for Ag201rto), the different deformation energies being minority (around 10% of $\tilde{\Gamma}_{coads}$). Hence, the $\tilde{\Gamma}_{coads}$ variations between different systems are determined by this contribution. The larger interaction energy gain found for Ag147ico is related to a larger contaminant surface density than those of *FCC* clusters. Indeed, for an equivalent coverage, the icosahedral cluster has the ability to coadsorb more methanethiol molecules on the same unit area, without losing too much in repulsion between them, thanks to its morphology. Those conclusions are not questioned by removing the pressure effect on the coadsorption structures optimized after MD simulations as shown in Figure 5.

4.4 Discussion

Different environment effects have been considered for modeling the impact of air exposure on Ag NPs (in the diameter range 1.66-1.80 nm). Both temperature and contaminant shell effects are predominant. Temperature determines the existence of a given morphology. Once a set of Ag NPs of various structures exists at a given temperature, the contaminant shells tune the competition between the nanoparticles through their interaction energy with the metal, and the contaminant surface density which is larger for icosahedral Ag147ico than for *FCC* Ag147sito and Ag201rto. The global effect of nitrogen pressure (of a few atm) is minority according to our study. However, in the presence of nitrogen gas at 300 K, only one contaminant has desorbed among 180 adsorbed methanethiol molecules on Ag NPs, during a total integration time of 35 ps along the AIMD trajectories. Hence methanethiol desorption is a rare event in our simulation conditions.

Regarding nanoclusters in vacuum, the excess energy normalized to the NP surface area and calculated at 0 K and 300 K, shows that *FCC* clusters are more favorable than the icosahedral one. The ino-decahedral cluster, which is found metastable at 0 K, transforms into other morphologies at both 300 and 600 K. Our results concerning the *FCC* and icosahedral nanoparticles are consistent with the predominance of *FCC* clusters demonstrated experimentally in vacuum and in the range 309-923 atoms.[19,20] According to these experimental works, the icosahedral shape is always minority whereas the decahedral forms become competitive with the *FCC* clusters at larger size (at sizes 742±17 and 923±21 atoms). Hence, the results of our AIMD simulations predict reasonably the experimental trends related to icosahedral *vs FCC* nanoparticles. Concerning the decahedral clusters, their increase in statistics with NP size would require a specific AIMD investigation of a large set of Marks-decahedral clusters, which will be the subject of a dedicated study.

Very recent measurements, conducted at room temperature and in the range 1-3000 atoms, have evidenced a significant change in morphology statistics upon air exposure.[21] In this experimental work, the Ag NPs have been first synthesized in vacuum and then exposed to air before characterisation. An increase of the statistics of icosahedral nanoparticles has been observed by comparison with measurements in vacuum.[19,20] An observation of prevailing icosahedral morphology had been previously reported for Ag NPs synthesized in solution.[22] In the recent and combined experimental and theoretical study,[21] a first element of explanation was proposed on the basis of static DFT models of methanethiol covered Ag NPs. The authors have shown a more exothermic Γ_{coads} for contaminated Ag147ico by comparison with *FCC* clusters of similar size. This preliminary theoretical model was certainly incomplete, since temperature and pressure effects were totally neglected. By the light of our AIMD simulations, these

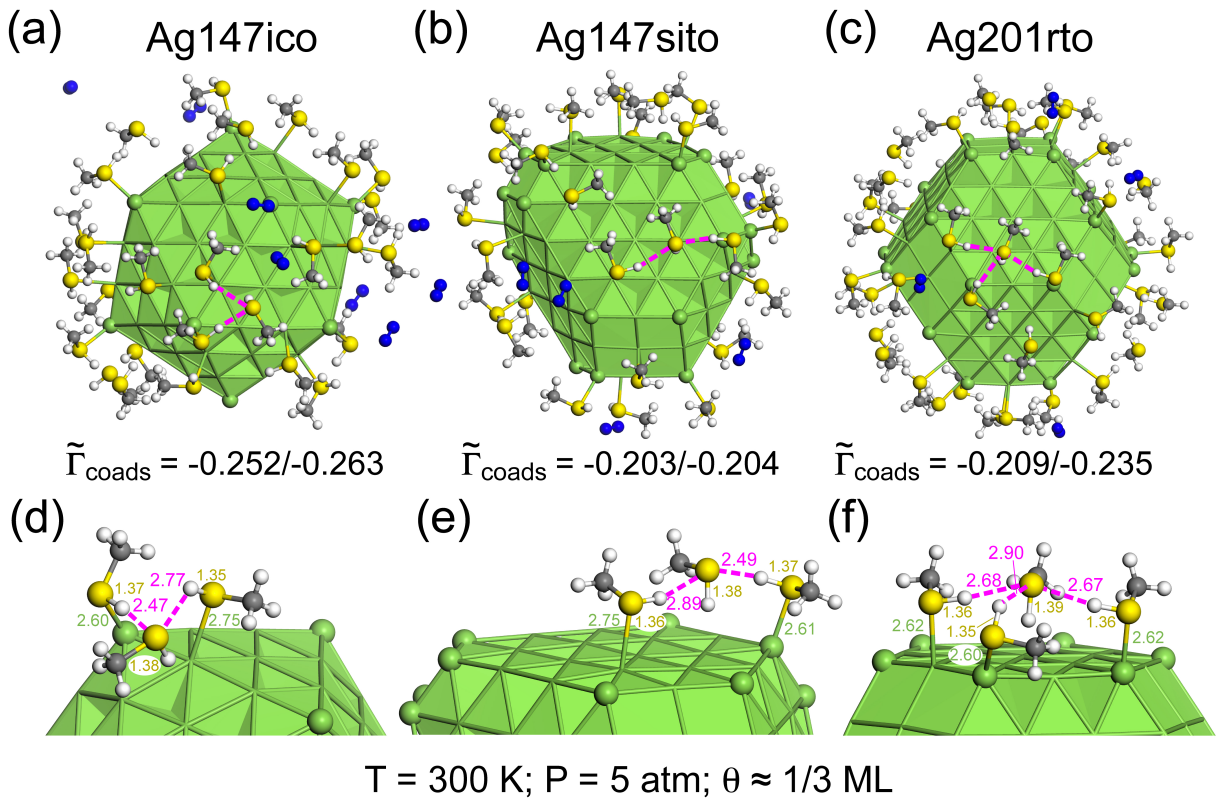

Fig. 4 Illustration of final structures for contaminated Ag NPs immersed in gaseous nitrogen (5 atm), equilibrated at 300 K, extracted from AIMD trajectories and optimized in accurate conditions. The numbers of contaminant molecules are identical to those exposed in Figure 2. Optimal structures of (a) Ag147ico (1_dyn14_step31 in Table 3), (b) Ag147sito (dyn3_step333 in Table 3) and (c) Ag201rto (2_dyn8_step286 in Table 3). In each case, an example of a coadsorption species composed of three or four methanethiol molecules is extracted from the optimized structures and depicted below them (d) Ag147ico (e) Ag147sito and (f) Ag201rto. In such coadsorption species, two or three methanethiol molecules are bound through hydrogen bonds (see the dotted pink lines) to one contaminant which is adsorbed on the Ag NP via one $Ag\cdots H-SCH3$ non-conventional hydrogen bond. Total coadsorption energies normalized to the nanoparticle surface area ($\tilde{\Gamma}_{coads}$, in J.m^{-2}) are reported with ranges of values corresponding to the coadsorption structures† reported in Table 3. Distances in figures (d)-(e)-(f) are given in Å. The color labels are identical to Figure 3. The color labels of distance values are defined as follows : green for Ag-S, yellow for S-H and pink for $S\cdots H$.

effects are to be considered in the models, in particular the temperature effect on Ag NP morphology (determining its existence) and on the reorganisation of adsorbed contaminant shells (generating more stable configurations). Our AIMD results at 300 K confirm the largest exothermicity for the contaminant shells adsorbed on icosahedral Ag147ico. These results support the very recent measurements of air-exposed Ag NPs.[21] Regarding the existence of the decahedral morphology, our AIMD study shows that the ino-decahedral shape is not stable at room temperature in vacuum, similarly with measurements conducted in solution and indicating the absence of decahedral clusters.[22] However, decahedral symmetry was detected when Ag NPs were exposed to air.[21] According to our study, these decahedral clusters should not be ino-decahedral forms but likely defective clusters such as Marks-decahedra, which were not considered so far.

According to our AIMD investigation, we have not registered the formation of ageing phases all along the trajectories (sulphides, carbides, hydrides, nitrides) under atmospheric pressure at room temperature. Hence, either our simulation time is not enough to observe this, or the interaction of the silver clusters with methanethiol and N_2 is not strong enough to promote such a transformation of Ag NPs, or additional contaminant molecules such as molecular oxygen or other organic pollutants should be included in the models. Moreover, we have not registered the formation of amorphous clusters when Ag NPs are exposed to air in the range 147-201 atoms. An amorphous Ag cluster had been previously observed from *ab initio* molecular dynamics by considering a smaller nanoparticle supported on alumina.[34] The authors had shown that in the temperature range 25-100 K, a Ag_{54} cluster in contact with this support can either stay crystalline or become amorphous.

From a static standpoint, it is interesting to compare the silver-silver distances in the optimal geometry of the icosahedral morphology in vacuum with the same cluster exposed to air. In a previous experimental study, a contraction of the lattice parameter in silver nanoparticles in vacuum or exposed to air was measured by comparison with the bulk value (below 1.2%), whatever the temperature in the range 0-700 °C. Such a contraction is less when the Ag NPs are exposed to air.[9] According to our analysis, we found that average metal-metal distance for Ag147ico is slightly larger in air (2.883 Å) than in vacuum (2.880 Å), in agreement with experiments. From the theoretical standpoint,

Table 3 Coadsorption structures extracted from AIMD simulations at 300 K and optimized in accurate conditions for contaminated Ag NPs (Ag147ico, Ag147sito and Ag201rto) in nitrogen gas. Name of coadsorption structure, number of corresponding figure†, number of methanethiol molecules in the adsorbed layer (N_{HSCH3}), average coadsorption energy ($\tilde{E}_{coads}$, eV/molec), average contribution of dispersion to coadsorption energy ($\tilde{E}^{disp}_{coads}$, eV/molec), total coadsorption energy normalized to nanoparticle surface area ($\tilde{\Gamma}_{coads}$, J.m^{-2}), interaction energy between Ag cluster and contaminant shell from energy decomposition analysis model ($\tilde{\Gamma}^{NP-shell}_{int}$, J.m^{-2}), deformation energy of Ag cluster upon interaction with contaminant shell ($\tilde{\Gamma}^{NP}_{def}$, J.m^{-2}).

NP	Coads. Structure	Figure†	N_{HSCH3}	$\tilde{E}_{coads}$	$\tilde{E}^{disp}_{coads}$	$\tilde{\Gamma}_{coads}$	$\tilde{\Gamma}^{NP-shell}_{int}$	$\tilde{\Gamma}^{NP}_{def}$
Ag147ico	1_dyn7_step264	S25	32	-0.590	-0.314	-0.254		
	1_dyn11_step444	S26	32	-0.592	-0.353	-0.254		
	1_dyn14_step31	S27	32	-0.611	-0.368	-0.263	-0.231	0.003
	2_dyn11_step456	S28	32	-0.585	-0.348	-0.252		
	2_dyn12_step288	S29	32	-0.593	-0.350	-0.255		
	2_dyn15_step59	S30	32	-0.607	-0.355	-0.261		
Ag147sito	dyn3_step333	S31	32	-0.625	-0.376	-0.204	-0.185	0.003
	dyn6_step771	S32	32	-0.619	-0.370	-0.203		
	dyn10_step1283	S33	32	-0.624	-0.367	-0.204		
Ag201rto	1_dyn10_step140	S34	40	-0.644	-0.368	-0.210		
	1_dyn12_step449	S35	40	-0.640	-0.363	-0.209		
	1_dyn15_step122	S36	40	-0.654	-0.379	-0.213		
	2_dyn8_step286	S37	44	-0.654	-0.392	-0.235	-0.210	0.003
	2_dyn8_step1030	S38	44	-0.639	-0.382	-0.229		
	2_dyn8_step1817	S39	44	-0.652	-0.394	-0.234		

the comparison between the bulk value (*FCC* packing) and the Ag147ico cluster is not straightforward since the *Ih* symmetry does not exist in the bulk. Besides, it is worth detailing this geometrical analysis by separating the optimized Ag-Ag distances in the shells of the core and the surface, and between the shells. For Ag147ico both in vacuum and in air, we have obtained larger Ag-Ag distances in the surface with respect to those in the core of the nanoparticle, in agreement with first simulations based on interatomic potentials.[40] At the opposite, other DFT models of Ag NPs clusters in the range 13-309 atoms showed a significant expansion of the core of the nanoparticle with respect to the surface.[35] Those predictions which were performed with SIESTA code and based on DFT-PBE calculations with a minimal double-ζ polarized basis set (without diffuse functions and without van der Waals interactions), are neither compatible with our plane-wave PBE-D3 calculations, nor with first conclusions based on interatomic potentials simulations.[40] Another interesting structural analysis element is the comparison of radial distribution functions (RDFs) of Ag NPs between vacuum and air, as presented on Figures S40-S42†, for Ag147ico, Ag147sito and Ag201rto, respectively. The environment effects are globally weak on the metallic structures. Only small variations are seen on the RDF in the case of Ag147sito at its surface. The preserved FCC crystallinity had already been mentioned in the literature from pair distribution functions (PDFs) calculated for large Ag NPs (365-1099 atoms) in vacuum.[27] Based on a Lennard-Jones interaction potential, the authors have also seen only weak surface modifications for a clean or a polymer-coated water-solvated cubic cluster Ag1099. The weak temperature impact on the PDFs has also been reported for large Ag NPs (5083 atoms).[53] This absence of large modifications observed from theoretical models of Ag crystalline clusters is ensured by comparison with measurements of liquid Ag PDFs.[54]
Regarding the adsorption of small molecules on silver nanoparticles in vacuum, a very recent DFT investigation on carbon monoxide adsorption on Ag NPs in the range 54-309 atoms showed that the adsorption strength is globally weak (from 0.2 to 0.6 eV/molec) and dominated by van der Waals forces (above 50 % starting from 147 atoms).[34] For methanethiol molecules, our adsorption strength on Ag NPs in the range 147-201 atoms is also moderate (from 0.43 to 0.70 eV/molec) with a similar dispersion contribution (32-73%). Hence the compatibility of our DFT results with state-of-the-art regarding adsorption strength and dispersion contributions to adsorption energetics of moderately bound contaminants validates our theoretical approach. Our study opens interesting perspectives in a more general context of the influence of gaseous environment on the morphology of various nanomaterials.[55,56]

5 Conclusion and perspectives

In this work, we have explored theoretical models of Ag NPs either in vacuum or exposed to air by dispersion-corrected DFT calculations and AIMD simulations performed at 300 and 600 K. Contaminated nanoparticles have been modeled by methanethiol covered Ag NPs of various morphologies under atmospheric pressure and at finite temperature.

In vacuum, icosahedral and regular truncated octahedral shapes (Ag147ico and Ag201rto) show a good stability at 300 and 600 K. The ino-decahedral shape (Ag147ino) is not stable at these temperatures, while the strongly irregular truncated octahedral shape (Ag147sito) is stable at 300 K and unstable at 600 K. The larger stability of the *FCC* form over the icosahedral shape has been demonstrated and agrees with measurements of Ag NPs protected from atmospheric exposure.

Concerning the morphology of the contaminated Ag clusters at 300 K, Ag147ico, Ag147sito and Ag201rto are found stable. No structural transition of the nanoparticle has been observed along the AIMD simulations, meaning that the moderate adsorption strength of methanethiol is not enough to induce any nanoparticle transformation, at a coverage below saturation. Our analysis

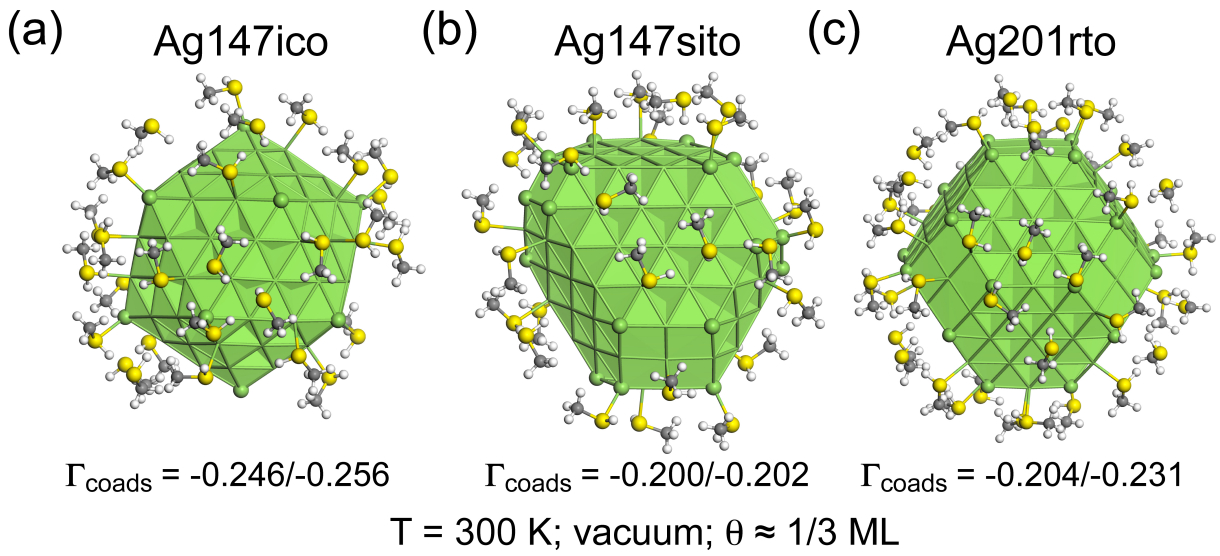

Fig. 5 Illustration of contaminated Ag NPs structures optimized at 0 K without gaseous nitrogen, in tight conditions. The initial structures were extracted from the AIMD simulations at 300 K and optimized at 0 K (see Figure 4 and Table 3) before removing nitrogen gas. (a) Ag147ico, (b) Ag147sito and (c) Ag201rto. Total coadsorption energies normalized to the nanoparticle surface area (Γ_{coads}, in J.m^{-2}) are reported with ranges of values corresponding to several coadsorption structures†. The color labels are identical to Figure 2.

concludes that, when Ag NPs are exposed to air, the contaminant adsorption is more stabilizing on Ag_{147} icosahedral cluster, by comparison with *FCC* forms of comparable size. This results is fully compatible with a very recent experimental study.[21]

For nanometric Ag NPs exposed to air at finite temperature and under atmospheric pressure, a moderate adsorption strength of surface contaminants below saturation is enough to modulate the relative statistics between symmetries in competition. This work paves the way to AIMD investigations, on one hand, of defective Ag NPs such as Marks-decahedra, and on the other hand, of more strongly bound contaminant species such as oxides and sulphides, in the context of the ageing mechanisms of Ag NPs. Our results would be also interesting for developments of parameterized DFT-based methods (such as Density-Functional based Tight-Binding DFTB) and machine learning methods.

Author Contributions

The authors have equally contributed to this work (Conceptualization, Data curation, Formal Analysis, Investigation, Methodology, Resources, Validation, Visualization, Writing – original draft, Writing – review editing).

Conflicts of interest

There are no conflicts to declare.

Acknowledgements

The authors thank Richard E. Palmer for having suggested to examine theoretical models on this topic and for fruitful discussions. The authors thank IDRIS in Paris, CINES in Montpellier, TGCC in Grenoble (project 609, GENCI/CT8) and PSMN in Lyon for CPU time and assistance. The authors thank the CPER/SYSPROD 2015-2022 project (N°2019-AURA-P5B) and AXELERA Pôle de Compétitivité (PSMN Data Center). This work was granted access to the HPC resources of CALMIP supercomputing center under the allocation [p1303].

Notes and references

1 A. Desireddy, B. E. Conn, J. Guo, B. Yoon, R. N. Barnett, B. M. Monahan, K. Kirschbaum, W. P. Griffith, R. L. Whetten, U. Landman and T. P. Bigion, Ultrastable silver nanoparticles, *Nature*, 2013, **501**, 399–402.

2 E. Izak-Nau, A. Huk, B. Reidy, H. Uggerud, M. Vadset, S. Eiden, M. Voetz, M. Himly, A. Duschl, M. Dusinska and I. Lynch, Impact of storage conditions and storage time on silver nanoparticles' physicochemical properties and implications for their biological effects, *RSC Advances*, 2015, **5**, 84172–84185.

3 O. Velgosova, E. Čižmárová, J. Málek and J. Kavuličova, Effect of storage conditions on long-term stability of Ag nanoparticles formed via green synthesis, *International Journal of Minerals, Metallurgy and Materials*, 2017, **24**, 1177–1182.

4 Y. Li and E. Cummins, Probabilistic risk assessment of AgNPs for human health through dietary consumptions of crops, *Environ. Sci.: Nano*, 2022, **9**, 3049.

5 V. Keast, Corrosion processes of silver nanoparticles, *Applied Nanoscience*, 2022, **12**, 1859.

6 M. Marchioni, C. Battocchio, Y. Joly, C. Gateau, S. Nappini, I. Pis, P. Delangle, I. Michaud-Soret, A. Deniaud and G. Veronesi, Thiolate-Capped Silver Nanoparticles: Discerning Direct Grafting from Sulfidation at the Metal–Ligand Interface by Interrogating the Sulfur Atom, *The Journal of Physical Chemistry C*, 2020, **124**, 13467–13478.

7 J. D. Padmos and P. Zhang, Surface Structure of Organosulfur Stabilized Silver Nanoparticles Studied with X-ray Absorption Spectroscopy, *The Journal of Physical Chemistry C*, 2012, **116**,

23094–23101.

8 C. Battocchio, C. Meneghini, I. Fratoddi, I. Venditti, M. V. Russo, G. Aquilanti, C. Maurizio, F. Bondino, R. Matassa, M. Rossi, S. Mobilio and G. Polzonetti, Silver Nanoparticles Stabilized with Thiols: A Close Look at the Local Chemistry and Chemical Structure, *The Journal of Physical Chemistry C*, 2012, **116**, 19571–19578.

9 J. Hu, W. Cai, C. Li, Y. Gan and L. Chen, In situ x-ray diffraction study of the thermal expansion of silver nanoparticles in ambient air and vacuum, *Applied Physics Letters*, 2005, **86**, 151915.

10 S. I. Sadovnikov and A. I. Gusev, Recent progress in nanostructured silver sulfide: from synthesis and nonstoichiometry to properties, *Journal of Materials Chemistry A*, 2017, **5**, 17676–17704.

11 S. I. Sadovnikov and E. Y. Gerasimov, Direct TEM observation of the "acanthite α-Ag2S–argentite β-Ag2S" phase transition in a silver sulfide nanoparticle, *Nanoscale Advances*, 2019, **1**, 1581–1588.

12 J. D. Padmos, R. T. M. Boudreau, D. F. Weaver and P. Zhang, Impact of Protecting Ligands on Surface Structure and Antibacterial Activity of Silver Nanoparticles, *Langmuir*, 2015, **31**, 3745–3752.

13 P. Korshed, L. Li, D. Ngo and T. Wang, Effect of Storage Conditions on the Long-Term Stability of Bactericidal Effects for Laser Generated Silver Nanoparticles, *Nanomaterials (Basel).*, 2018, **8**, 218.

14 O. Wetzel, S. Hosseini, K. Loza, M. Heggen, O. Prymak, P. Bayer, C. Beuck, T. Schaller, F. Niemeyer, C. Weidenthaler and M. Epple, Metal–Ligand Interface and Internal Structure of Ultrasmall Silver Nanoparticles (2 nm), *The Journal of Physical Chemistry B*, 2021, **125**, 5645–5659.

15 M. Kaushik, A. Y. Li, R. Hudson, M. Masnadi, C.-J. Li and A. Moores, Reversing aggregation: direct synthesis of nanocatalysts from bulk metal. Cellulose nanocrystals as active support to access efficient hydrogenation silver nanocatalysts, *Green Chemistry*, 2016, **18**, 129–133.

16 J. Yan, J. Zhang, X. Chen, S. Malola, B. Zhou, E. Selenius, X. Zhang, P. Yuan, G. Deng, K. Liu, H. Su, B. K. Teo, H. Häkkinen, L. Zheng and N. Zheng, Thiol-stabilized atomically precise, superatomic silver nanoparticles for catalysing cycloisomerization of alkynyl amines, *National Science Review*, 2018, **5**, 694–702.

17 H. Yang, Y. Wang, X. Chen, X. Zhao, H. H. Lin Gu, J. Yan, C. Xu, G. Li, unchao Wu, A. J. Edwards, B. Dittrich, Z. Tang, D. Wang, L. Lehtovaara, H. Häkkinen and N. Zheng, Plasmonic twinned silver nanoparticles with molecular precision, *Nature Commununication*, 2016, **7**, 12809.

18 A. Campos, N. Troc, E. Cottancin, M. Pellarin, H.-C. Weissker, J. Lermé, M. Kociak and M. Hillenkamp, Plasmonic quantum size effects in silver nanoparticles are dominated by interfaces and local environments, *Nature Physics*, 2019, **15**, 275.

19 D. M. Foster, Production and characterisation by scanning transmission electron microscopy of size-selected noble metal nanoclusters, *University of Birmingham. Ph.D.*, 2017.

20 D. Loffreda, D. M. Foster, R. E. Palmer and N. Tarrat, Importance of Defective and Nonsymmetric Structures in Silver Nanoparticles, *The Journal of Physical Chemistry Letters*, 2021, **12**, 3705–3711.

21 J. Vernieres, N. Tarrat, S. Lethbridge, E. Watchorn-Rokutan, T. Slater, D. Loffreda and R. E. Palmer, Influence of air exposure on structural isomers of silver nanoparticles, *Communications Chemistry*, 2023, **6**, 19.

22 N. Jian and R. E. Palmer, Variation of the Core Atomic Structure of Thiolated $(Au_xAg_{1-x})_{312\pm55}$ Nanoclusters with Composition from Aberration-Corrected HAADF STEM, *The Journal of Physical Chemistry C*, 2015, **119**, 11114–11119.

23 J. Wen and J. Ma, The role of substrate in packing structures of sexithiophenes on Ag(111) surface: molecular dynamics simulations and quantum chemical calculations, *Journal of Theoretical and Computational Chemistry*, 2009, **08**, 677–690.

24 P. S. Mdluli, N. M. Sosibo, P. N. Mashazi, T. Nyokong, R. T. Tshikhudo, A. Skepu and E. van der Lingen, Selective adsorption of PVP on the surface of silver nanoparticles: A molecular dynamics study, *Journal of Molecular Structure*, 2011, **1004**, 131–137.

25 H. Heinz, T.-J. Lin, R. Kishore Mishra and F. S. Emami, Thermodynamically Consistent Force Fields for the Assembly of Inorganic, Organic, and Biological Nanostructures: The INTERFACE Force Field, *Langmuir*, 2013, **29**, 1754–1765.

26 A. Kyrychenko, O. M. Korsun, I. I. Gubin, S. M. Kovalenko and O. N. Kalugin, Atomistic Simulations of Coating of Silver Nanoparticles with Poly(vinylpyrrolidone) Oligomers: Effect of Oligomer Chain Length, *The Journal of Physical Chemistry C*, 2015, **119**, 7888–7899.

27 M. M. Blazhynska, A. Kyrychenko and O. N. Kalugin, Molecular dynamics simulation of the size-dependent morphological stability of cubic shape silver nanoparticles, *Molecular Simulation*, 2018, **44**, 981–991.

28 M. M. Blazhynska, A. V. Kyrychenko and O. N. Kalugin, Polarizable force field for molecular dynamics simulations of silver nanoparticles, *Kharkiv University Bulletin. Chemical Series*, 2019, 46–58.

29 J. P. K. Doye and F. Calvo, Entropic Effects on the Size Dependence of Cluster Structure, *Physical Review Letters*, 2001, **86**, 3570–3573.

30 F. Baletto, C. Mottet and R. Ferrando, Microscopic mechanisms of the growth of metastable silver icosahedra, *Physical Review B*, 2001, **63**, 155408.

31 F. Baletto, R. Ferrando, A. Fortunelli, F. Montalenti and C. Mottet, Crossover among structural motifs in transition and noble-metal clusters, *The Journal of Chemical Physics*, 2002, **116**, 3856–3863.

32 X. Shao, X. Yang and W. Cai, Geometry optimization and structural distribution of silver clusters from Ag_{170} to Ag_{310}, *Chemical Physics Letters*, 2008, **460**, 315–318.

33 J. M. Rahm and P. Erhart, Beyond Magic Numbers: Atomic Scale Equilibrium Nanoparticle Shapes for Any Size, *Nano Letters*, 2017, **17**, 5775–5781.

34 K. Sawabe and A. Satsuma, Theoretical Study on Carbon Monoxide Adsorption on Unsupported and γ-Al2O3-Supported Silver Nanoparticles: Size, Shape, and Support Effects, *ACS Omega*, 2022, **7**, 4405–4412.

35 D. Becerril and C. Noguez, Adsorption of a Methylthio Radical on Silver Nanoparticles: Size Dependence, *The Journal of Physical Chemistry C*, 2015, **119**, 10824–10835.

36 Y. Akinaga, T. Nakajima and K. Hirao, A density functional study on the adsorption of methanethiolate on the (111) surfaces of noble metals, *The Journal of Chemical Physics*, 2001, **114**, 8555–8564.

37 F. P. Cometto, P. Paredes-Olivera, V. A. Macagno and E. M. Patrito, Density Functional Theory Study of the Adsorption of Alkanethiols on Cu(111), Ag(111), and Au(111) in the Low and High Coverage Regimes, *The Journal of Physical Chemistry B*, 2005, **109**, 21737–21748.

38 H. Yang, Y. Wang, H. Huang, L. Gell, L. Lehtovaara, S. Malola, H. Häkkinen and N. Zheng, All-thiol-stabilized Ag_{44} and $Au_{12}Ag_{32}$ nanoparticles with single-crystal structures., *Nature Communications*, 2013, **4**, 2422.

39 S. Malola, P. Nieminen, A. Pihlajamäki, J. Hämäläinen, T. Kärkkäinen and H. Häkkinen, A method for structure prediction of metal-ligand interfaces of hybrid nanoparticles., *Nature Communications*, 2019, **10**, 3973.

40 C. Mottet, G. Tréglia and B. Legrand, New magic numbers in metallic clusters: an unexpected metal dependence, *Surface Science*, 1997, **383**, L719–L727.

41 G. Kresse and J. Hafner, Ab initio molecular dynamics for liquid metals, *Physical Review B*, 1993, **47**, 558–561.

42 G. Kresse and J. Furthmüller, Efficiency of ab-initio total energy calculations for metals and semiconductors using a plane-wave basis set, *Computational Materials Science*, 1996, **6**, 15–50.

43 G. Kresse and J. Furthmüller, Efficient iterative schemes for ab initio total-energy calculations using a plane-wave basis set, *Physical Review B*, 1996, **54**, 11169–11186.

44 S. Grimme, J. Antony, S. Ehrlich and H. Krieg, A consistent and accurate ab initio parametrization of density functional dispersion correction (DFT-D) for the 94 elements H-Pu, *The Journal of Chemical Physics*, 2010, **132**, 154104.

45 G. Kresse and D. Joubert, From ultrasoft pseudopotentials to the projector augmented-wave method, *Physical Review B*, 1999, **59**, 1758–1775.

46 M. Blackman, N. D. Lisgarten and L. M. Skinner, Surface Energy and Evaporation Rate of Spherical Particles of Radii less than 500 Å, *Nature*, 1968, **217**, 1245–1246.

47 K. K. Nanda, A. Maisels, F. E. Kruis, H. Fissan and S. Stappert, Higher Surface Energy of Free Nanoparticles, *Physical Review Letters*, 2003, **91**, 106102.

48 S. Klacar, A. Hellman, I. Panas and H. Grnbeck, Oxidation of Small Silver Clusters: A Density Functional Theory Study, *The Journal of Physical Chemistry C*, 2010, **114**, 12610–12617.

49 A. H. Hakimioun, E. M. Dietze, B. D. Vandegehuchte, D. Curulla-Ferre, L. Joos, P. N. Plessow and F. Studt , Theoretical Investigation of the Size Effect on the Oxygen Adsorption Energy of Coinage Metal Nanoparticles., *Catalysis Letters volume*, 2021, **151**, 3165–3169.

50 W.-X. Li, C. Stampfl and M. Scheffler, Oxygen adsorption on Ag(111): A density-functional theory investigation, *Phys. Rev. B*, 2002, **65**, 075407.

51 A. A. Peterson, L. C. Grabow, T. P. Brennan, B. Shong, C. Ooi, D. M. Wu, C. W. Li, A. Kushwaha, A. J. Medford, F. Mbuga, L. Li and J. K. Nørskov, Finite-Size Effects in O and CO Adsorption for the Late Transition Metals, *Topics in Catalysis*, 2012, **55**, 1276–1282.

52 C. J. Mize, L. D. Crosby, S. B. Isbill and S. Roy, Insight into Subsurface Adsorption Derived from a Lattice-Gas Model and Monte Carlo Simulations, *The Journal of Physical Chemistry C*, 2022, **126**, 5343–5353.

53 L. Medrano and C. Landauro, Influence of chemical disorder on the electronic level spacing distribution of the Ag_{5083} nanoparticle: A tight-binding study, *Physica B: Condensed Matter*, 2013, **412**, 122–125.

54 Z.-A. Tian, R.-S. Liu, H.-R. Liu, C.-X. Zheng, Z.-Y. Hou and P. Peng, Molecular dynamics simulation for cooling rate dependence of solidification microstructures of silver, *Journal of Non-Crystalline Solids*, 2008, **354**, 3705–3712.

55 A. R. Symington, R. M. Harker, M. T. Storr, M. Molinari and S. C. Parker, Thermodynamic Evolution of Cerium Oxide Nanoparticle Morphology Using Carbon Dioxide, *The Journal of Physical Chemistry C*, 2020, **124**, 23210–23220.

56 A. R. Symington, M. Molinari, S. Moxon, J. M. Flitcroft, D. C. Sayle and S. C. Parker, Strongly Bound Surface Water Affects the Shape Evolution of Cerium Oxide Nanoparticles, *The Journal of Physical Chemistry C*, 2020, **124**, 3577–3588.